$Co(OH)_2@MnO_2$ nanosheet arrays as hybrid binder free electrode for high performance lithium-on battery and Supercapacitor

Manab Kundu[#*], Gurvinder Singh, and Ann Mari Svensson[*]

Department of Material Science and Engineering, Norwegian University of Science and Technology (NTNU), NO-7491 Trondheim, Norway
#Present address: SRM Research Institute, Department of Chemistry, SRM Institute of Science and Technology, Kattankulathur, Chennai 603 203, India.

[*]Corresponding Author's

E-mail: manab.kundu@ntnu.no and annmari.svensson@ntnu.no

TEL: +4773593965

Abstract:

$Co(OH)_2@MnO_2$ nanosheet arrays were directly grown on nickel foam by two-step electrodeposition method with subsequent heat treatment at 170 ^oC. The hybrid electrode, where the electrodeposited $Co(OH)_2$ and MnO_2 nanosheets were inlayed with each other, and employed as binder free anode material for lithium-ion battery (LIB) and electrode for super capacitor (SC). For both application: LIB and SC, the $Co(OH)_2@MnO_2$ nanosheet electrode exhibited appreciable cycling stability with high specific capacity as well as specific capacitance and rate capability. The excellent electrochemical performances of this hybrid nanosheets electrode were probably ascribed to their unique 3D architecture which provides large active sites for efficient electrochemical reactions, and the synergistic effects of the two active materials. The electrodeposition method appears to be suitable for fabrication of binder-free, nanostructured, hybrid arrays, and as demonstrated here the $Co(OH)_2@MnO_2$ nanosheet could potentially be used as high-performance LIB and SC electrode material.

Introduction

The present state of art lithium-ion batteries (LIBs) and super capacitors (SCs) have emerged as the preferred energy storage technologies for portable electronics, stationary energy storage and all electric (EVs) as well hybrid electric vehicles (HEVs), in addition to a range of specialized applications in sensors and other measurement devices. Still, there are numerous challenges to be solved with these technologies, related to more environmentally friendly materials and fabrication, cost, life-time as well as energy and power density. For meeting these requirements, transition metal oxides have been intensively exploited as potential electrode materials owing to their higher theoretical capacity and capacitance values [1-4].

Unfortunately, challenges like their inherent low electric conductivity results in unsatisfactory supercapacitor performance and enormous volume change during lithiation/de-lithiation processes leading to poor cycling stability [5, 6]. In order to cope with these problems, one effective strategy is to design hybrid structures by integrating different metal oxides. These hybrid electrodes have many competitive advantages such as high electron/ion diffusion efficiency, rich accessible electroactive sites, improved cycle life and superior rate performance due to the synergetic effects between the two components [7, 8]. Moreover , these hybrid electrodes will show enhanced properties which are difficult to realize in a single component, such as the ability to buffer the volume changes and to react with large number of lithium ion reversibly. Hence, in the hybrid electrodes can take advantage of both components and offer special properties through a reinforcement or modification of each other. Therefore, a range of hybridized nanostructures including $FeCo_2O_4@MnO_2$, $MnCo_2O_4@MnO_2$, SnO_2/NiO $CoSe_2/Ni_{0.85}Se$, NiS/Ni_3S_4, $Ni_3S_2@Ni(OH)_2$ etc. have been intensively studied [9-14].

Another approach is to fabricate electrodes with a unique 3D architecture such as nanosheets directly grown on the current collector with desired mesoporosity [15, 16]. These binder free nanosheets with enhanced structural integrity have demonstrated superior rate capability by providing high accessible surface area, and promoting Li^+ and electron transport across the nanosheets [17, 18]. Moreover, the open space among the interconnected nanosheet structure can buffer volume change during electrochemical charge/discharge and facilitate the access to electrochemically active sites [19, 20]. The presence of well-defined pores on the surface of hybrid array favor better exposure of active sites and easier electrolyte access. Furthermore, by direct growth on current-collector, the electrical resistance of the binder can be avoided, and promote fast electron transport to current collector which improves the supercapacitive properties of the electrode. For example, Fan et al. [21] deposited porous Mn_3O_4 nanosheet arrays on porous Cu and used as binder free anode for LIB. These electrodes exhibited a reversible capacity of 667.9 mA h g^{-1} even after 1000 cycles at 1.0 A g^{-1} . Zhou et al. demonstrated the excellent lithium storage properties of vertically aligned MoS_2 nanosheets on a Ti substrate [22]. In another recent report, Chen and his co-workers demonstrated Mo-doped SnS_2 nanosheets grown on carbon cloth [23]. This Mo-doped SnS_2 nanosheet anode coupled with $LiCoO_2$ cathode also delivered high capacity and cycling stability. In some other reports, the excellent electrochemical performances of many binder free anodes such as stainless steel@Mn_3O_4 nanoflower [24], NiMn @Ni_3S_2 [25] and mesoporous $ZnCo_2O_4$ nanosheets [26], and $NiCo_2S_4$ nanosheets [27] has been reported.

In this work, we report on the design of an advanced electrode architecture of $Co(OH)_2$@MnO_2 nanosheet (NS) arrays grown on Nickel foam by electrodeposition, where the NSs are interconnected laterally, forming a highly open and porous structure, and firmly adhere to the underlying Ni foam. These arrays are further investigated with respect to

application as electrodes for supercapacitors and lithium ion batteries. The thin NSs with surface porosity can better accommodate the stress due to the volume changes during lithiation/delithiation process. This advanced architecture can shorten the path lengths for electronic and ionic transport. As anticipated, in view of the aforesaid superior properties, the bicomponent NSs displayed high specific capacity and capacitance, improved rate capability, and good cycling stability in both the lithium ion cell and the supercapacitor applications. Therefore, our result demonstrated that the binder free $Co(OH)_2$@MnO_2 NSs electrode has great potential as next generation LIB anode and SC electrode.

Experimental

$Co(OH)_2$ NSs were deposited by electrodeposition, which was performed in a standard three-electrode system using an electrochemical workstation (Biologic VMP3), a piece of Nickel foam (NF) as working electrode, a Pt sheet as the counter electrode, and a saturated calomel electrode (SCE) as the reference electrode. The electrolyte was a mixture of 0.05 M aqueous solutions of $Co(NO_3)_2$ and 0.1 M $NaNO_3$ (10:1 volume ratio). The deposition was carried out at a current constant density of 10 mA cm^{-2} for 5 min. Then the electrodeposited NFs were rinsed with distilled water and dried at 50 ^oC under vacuum overnight.

In order to deposit MnO_2, the $Co(OH)_2$ nanosheets covered NF was used as the working electrode, a platinum wire as counter electrode and 0.05 M manganese acetate (Sigma Aldrich, analytical grade) aqueous solution as electrolyte. The electrodeposition was conducted at room temperature at a constant voltage of 3 V for 1 min using a power supply (Nortelco AS, Norway). After deposition, the Ni foam was thoroughly rinsed with de-ionized water and heated at 170 ^oC for 5 hours. The mass loading of deposited nanosheets was in the range 1.1-1.5 mg cm^{-2}.

Field emission scanning electron microscopy (FE-SEM) images were collected using Zeiss Ultra 55 LE. Transmission electron microscopy images (TEM) were collected from JEOL2100 microscope operating at 200kV and Hitachi S5500 microscope operating at 30kV. Samples for TEM analysis were prepared by dispersing the materials in ethanol after scratching from Ni foam and drop 50 µl over formvar Cu TEM grid. In order to get X-ray diffraction patterns (XRD), the deposited nanosheets were scratched from the nickel foam surface. Bruker Da Vinci2 diffractometer with Cu Kα radiation (λ=1.5418 Å) was used for collecting XRD patterns. X-ray photoelectron spectroscopy (XPS) analyses were performed using a Kratos Axis Ultra DLD spectrometer (Kratos Analytical, UK), equipped with a monochromatized aluminum X-ray source (Al, hυ = 1486.6 eV) operating at 10 mA and 15 kV (150 W).

The electrochemical performance for application as battery electrodes was evaluated by cyclic voltammetry (CV), galvanostatic charge/discharge technique and electrochemical impedance spectroscopy (EIS) using a Biologic VMP3 battery tester. The tests were made using 2016 type coin cells with the Ni foam supported $Co(OH)_2@MnO_2$ NSs array as working electrode and Li metal as counter electrode. The electrolyte consists of $LiPF_6$ dissolved in EC: DEC (1:1 vol%). Celgard 2400 membranes were used as separator. The cells were assembled in an argon filled glove box (MBRAUN, Germany) where the moisture and oxygen levels were kept below 0.1 ppm.

The assessment of supercapacitive performance of the hybrid electrodes in aqueous solution was carried out in a three-electrode electrochemical cell using the mesoporous NSs array as working electrode, a platinum wire as counter electrode and Ag/AgCl as reference electrode. The electrochemical performance was evaluated by cyclic voltammetry (CV), and galvanostatic charge-discharge technique using a Biologic VMP3 battery tester. All the tests

were made at room temperature in a 3 M KOH aqueous solution. The potential window was 0 to 0.45 V (vs. Ag/AgCl). Specific capacitances were calculated using the equation below:

$$C = \frac{I\Delta t}{m\Delta V} \quad \text{(I)}$$

Where I is the discharge current, Δt is the discharging time, ΔV is the potential window, and m is the mass of the active material.

Results and Discussion.

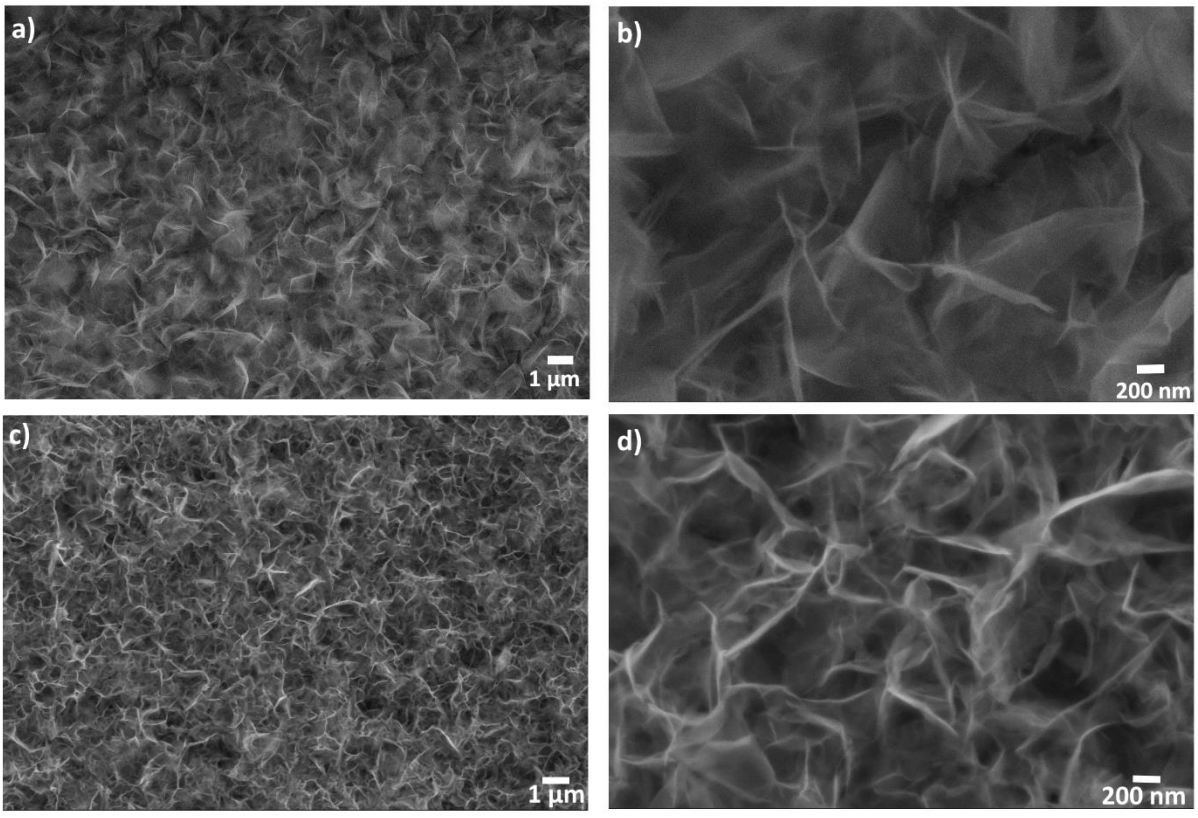

Figure1. FE-SEM images: (a and b) for $Co(OH)_2$ and (c and d) for the $Co(OH)_2@MnO_2$ NSs networks on the Ni

FE-SEM was employed to investigate the morphology and microstructure of the electrodeposited electrodes. Fig. 1 displays the FE-SEM images of the as-deposited $Co(OH)_2$ and $Co(OH)_2@MnO_2$ NS networks on the Ni foam substrates. As seen in low-magnification FE-SEM images in the Fig. 1(a, c), NS are grown uniformly on the Ni foam substrate. Fig. 1b, d show the high-magnification FE-SEM images of $Co(OH)_2$ and $Co(OH)_2@MnO_2$ NSs arrays. It is observed that, in both cases, all the NSs are interconnected with each other forming a three dimensional network. Such architectures would allow Li-ion and electrolyte to access the active materials from both sides of the nanosheets and facilitate the fast ion and electron transportation. In the same time, the open space between the nonsheets will act as buffer space to alleviate the volume change during the electrochemical process.

Figure 2a shows electrochemically deposited $Co(OH)_2$ NS over nickel (Ni) foam. The sheet appears to be very thin because of its transparent behaviour under electron beam. High resolution TEM images and its Fourier transform (FT) indicate the formation of a crystalline sheet over Ni foam (Figure 2a). The measured interplanar spacing (~0.43 nm) corresponds to (100) plane and matched with hexagonal $Co(OH)_2$. EDS analysis was performed to confirm the chemical composition of the sheet. The results showed that the sheet is formed from oxygen (O) and Co (Figure 2c). The presence of copper (Cu) and carbon (C) peaks in the spectrum come from the Cu TEM grid.

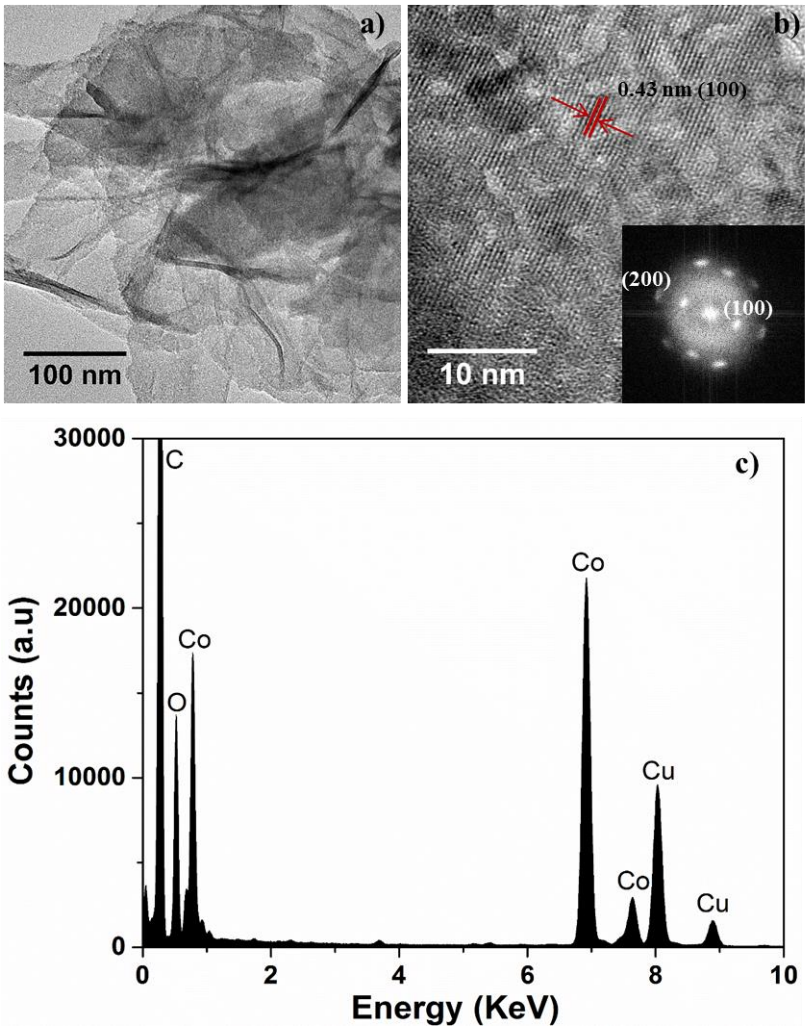

Figure 2. a) TEM image of $Co(OH)_2$ NS grown over nickel foam, b) high resolution TEM of $Co(OH)_2$ NS (inset is FT pattern) and c) EDS (energy dispersive spectroscopy) spectrum of sheet.

We synthesized a core@shell sheet by depositing a layer of MnO_2 NS over the $Co(OH)_2$ NS /Ni foam. The transparent nature of core@shell NS sheet confirms that the NS remained thin even after the deposition of MnO_2 (Figure 3a). The grown MnO_2 NS is also crystalline in nature as it is evident by high resolution and its FFT pattern. A careful FT analysis indicates the cubic structure of MnO_2 i.e., equal distance of six bright spots from the centre spot. Furthermore, the measured interplanar spacing (0.46 nm) correspond to the (111) plane,

which also match the cubic MnO_2 phase. The chemical composition of the core@shell sheet was analysed with TEM-EDS. Figure 3c shows EDS spectrum confirming the presence of Mn and Co peaks. The cross-sectional line profile of core@shell NS sheet also revealed the presence of Mn and Co (Figure 4a). The elemental mapping analysis showed the uniform distribution of Co and Ni in the sheet (Figure 4b). This rules out the possibility of surface segregation of atoms after the deposition of MnO_2 and subsequent heat treatment.

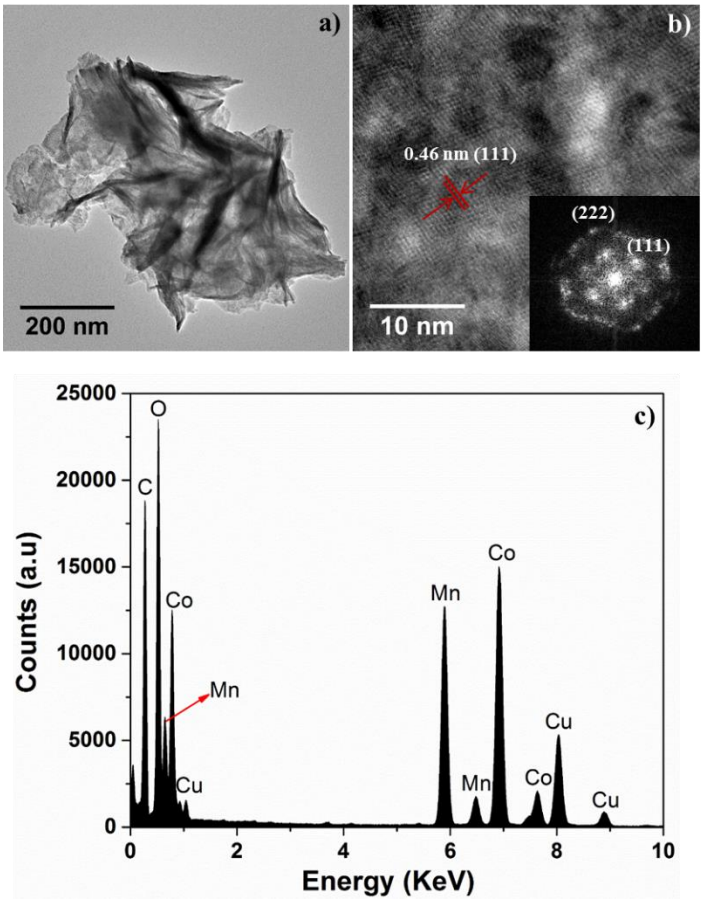

Figure 3. a) TEM image of MnO_2 NSs grown over $Co(OH)_2$ NSs deposited on nickel (Ni) foam, b) high resolution TEM of MnO_2 NSs (the inset is FT pattern) and c) EDS (energy dispersive spectroscopy) spectrum of sheet.

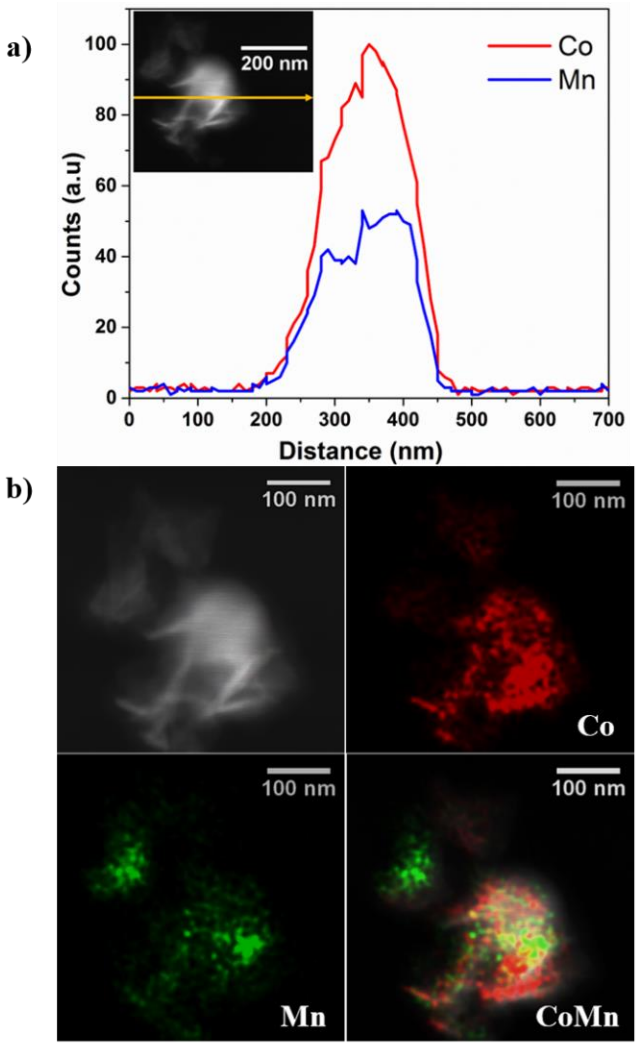

Figure 4. a) EDS line profile the sheet (inset is the dark field TEM image of the sheet) and **b)** dark field STEM-EDS elemental mapping of Co and Mn in the NSs grown over Ni foam. (STEM: scanning transmission electron microscopy).

Figure 5 shows XRD pattern for MnO_2 NSs electrodeposited over $Co(OH)_2$ NSs/Ni. The peaks at 2θ values of 31.24, 36.30, 54.19, 56.19 and 64.96 corresponds to the phase ε-MnO_2 (PDF: 00-012-0141) as indicated by * in Figure 5. The peaks at other 2θ values originate from background substrates (*i.e* $Co(OH)_2$/Ni substrate). For comparison, XRD pattern of $Co(OH)_2$ NSs/Ni is presented in Figure S1, where peaks are ell agreement with the $Co(OH)_2$.

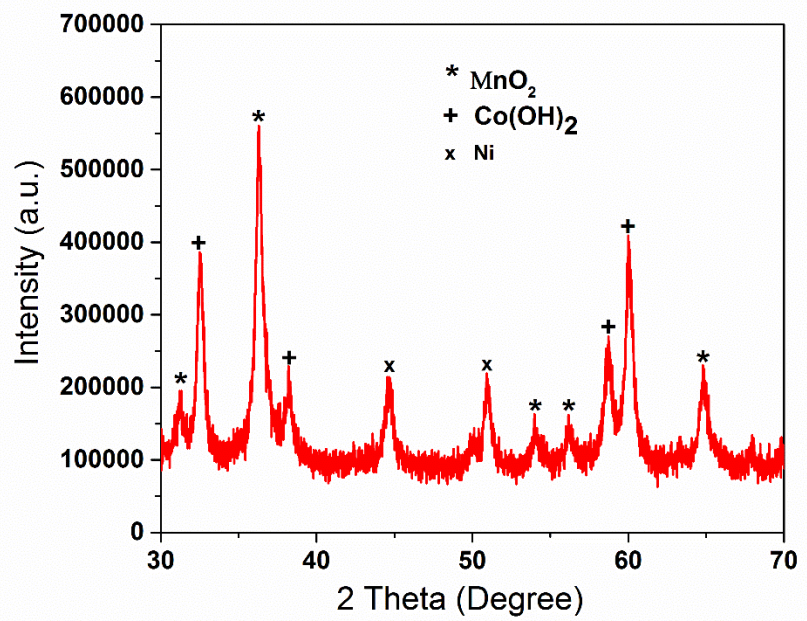

Figure 5. XRD pattern of electrodeposited $Co(OH)_2$@MnO_2 NSs.

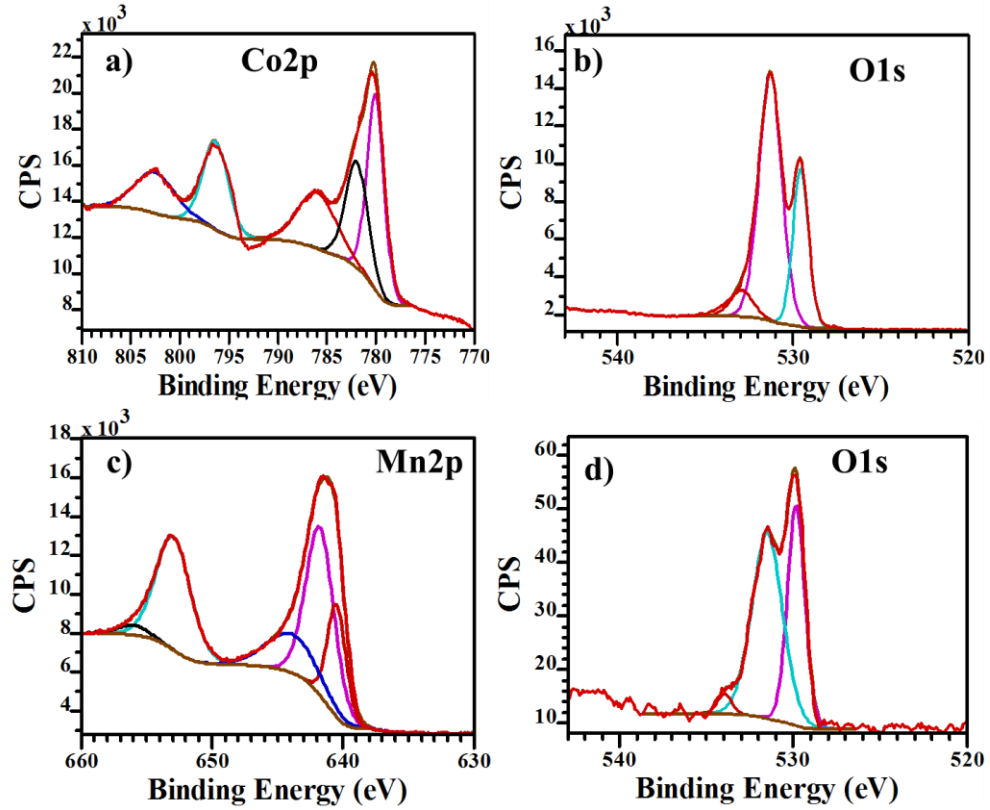

Figure 6. XPS spectra of electrodeposited $Co(OH)_2$ NSs: a) Co 2p and b) O1s. XPS spectra of electrodeposited $Co(OH)_2$@MnO_2 NSs: c) Mn 2p and d) O1s.

To investigate the chemical state of electrodeposited $Co(OH)_2$ and $Co(OH)_2@MnO_2$ NSs, X-ray photoelectron spectroscopy (XPS) was used. In the high-resolution XPS spectrum of Co 2p, five deconvoluted peaks at 780.1, 782.1, 786.2, 796.4 and 802.8 eV are attributed to the existence of Co^{2+} reported for $Co(OH)_2$ in the literature (Figure 6a) [28, 29]. The broad shoulders at 786.2 and 802.8 eV are satellite peaks, which are always observed in the 3d transition metal compounds. In the O1s spectrum, the main peak cantered at 531.2 eV corresponds to OH bonding to Co(II) , and two additional intensity peaks at lower and high binding energies *i.e* 529.5 and 532.9 eV can be assigned to CoO and OH, respectively [28, 29] (Figure 5b). For electrodeposited $Co(OH)_2@MnO_2$ NSs, the high-resolution XPS spectrum of Mn 2p can be fitted with five peaks (Figure 6c). In this spectrum, the main peaks centred at 642.1 and 653.2 eV can be attributed to the presence of Mn^{4+} in MnO_2 [29, 30]. The peak at lower binding energy (640.6 eV) can be assigned to the presence of Mn^{2+}, however the intensity of this peak is relatively low compared to peaks at 642.1 and 653.2 eV, indicating the dominant chemical state of Mn^{4+} in the electrodeposited MnO_2 film. The broad and weak shoulder peaks at higher binding energies (644.4 and 656.2 eV) are satellite peaks attributed to Mn^{4+} state. The three peaks at binding energies of 529.8, 531.5 and 534.1 eV in the high-resolution spectrum of O1s can be assigned to Mn-O-Mn, Mn-OH and OH [30] (Figure 6d).

In order to evaluate the electrochemical performance with respect to application in lithium-ion batteries, the electrodeposited $Co(OH)_2$ and $Co(OH)_2@MnO_2$ NSs anode were directly used as the binder-free electrodes. Figure 7a and b shows the CV curves of the $Co(OH)_2$ and $Co(OH)_2@MnO_2$ NSs electrode for the first four cycles in the potential range from 3.0 to 0.0 V (vs Li^+/Li) at a scan rate of 0.2 mV s^{-1}. The quite different curves shapes and redox peaks of these two electrodes clearly demonstrate the MnO_2 nanosheets play a significant role in the electrochemical performance.

In Figure 7a, in the first lithiation process, a strong reduction peak with a shoulder, at around 0.8 V is observed. This peak corresponds to the formation of the SEI layer (irreversible), as well as the reduction of $Co(OH)_2$ to Co [31]. During the delithiation process, two oxidation peaks at 1.44 V and 2.16 V are associated with the oxidation of Co to Co^{2+}. In the second and third cycle, the reduction peak associated with the formation of SEI layer disappears, as expected. Meanwhile, a new reduction peak appears around 1.3 V, which indicate that a new lithiation process has been activated, as the peak remains in the subsequent cycles. The exact reason for this activation is not known, but it has previously been shown that nanosized α-Fe_2O_3 would undergo more lithiation steps compared to micronsized α-Fe_2O_3 [32]. Recently, Zhou et al. suggested different lithium storage mechanism of nanosized $Co(OH)_2$ because of its high surface area [33]. However to establish this fact, further investigation is need. In the third and fourth cycles, the overlap of the voltammogrmas suggest good reversibility and stability of the electrochemical reactions. The cyclic voltammograms are in good agreement with those previously reported work on $Co(OH)_2$ [33].

Figure 7b shows the CV for $Co(OH)_2$@MnO_2 NSs, where reduction peaks during the first cycle at 0.75 V corresponds to the formation of the SEI layer, at 0.6 V to the reduction of $Co(OH)_2$, whereas the additional peaks at 0.26 V and 0.1 V (first cycle only) are attributed to the reduction of MnO_2 [19]. The presence of additional reduction peaks of MnO_2 in the CV of $Co(OH)_2$@MnO_2 NSs indicates that $Co(OH)_2$ core of $Co(OH)_2$@MnO_2 NSs structure taking part in electrochemical reaction with Li. The similar behavior was also observed for some other hybrid anode such as $Ni(OH)_2$@MnO_2 NSs arrays on nickel foams [34].

Figure 7 c and d shows the 1st, 2nd, 3rd, and 10th charge discharge profiles $Co(OH)_2$ and $Co(OH)_2$@MnO_2 NSs, at a current density of 250 mA g^{-1}. The specific lithiation and delithiation capacity of $Co(OH)_2$ NSs during its initial cycle was determined to be 1464.64 and 1007 mAh g^{-1} corresponding to Coulombic efficiency of 68.75%. At the same time, the

specific lithiation and delithiation capacity of $Co(OH)_2@MnO_2$ NSs yielded a comparatively higher value of 1621.33 and 1134.67 mAh g^{-1} corresponding to Coulombic efficiency of 70 %. The irreversible capacity loss during the initial cycles in both electrodes is mainly due to the formation of a solid electrolyte interface (SEI) layer, related to decomposition of the electrolyte, and is rather high due to the high surface area of the electrode. Furthermore, the cycling performances at the corresponding current density of the both electrodes are shown in Figure 7d. From the Figure 7d it is clear that irrespective the electrode, after initial cycle the Coulombic efficiency increases with cycle number and reached almost 99%. The cycling stability and specific capacity of $Co(OH)_2@MnO_2$ NSs electrode is excellent compared to $Co(OH)_2$ NSs electrode.

A rate capability study of a $Co(OH)_2@MnO_2$ NSs electrode and $Co(OH)_2$ NSs electrode can be seen in Figure 8a, carried out at various current densities ranging from 50 mA g^{-1} to 1000 mA g^{-1}. The achievable average specific reversible capacity values of $Co(OH)_2@MnO_2$ NSs electrode are 1017.6, 916.5, 690.0, 526.6, 414 and 352.9 mAh g^{-1} at the current densities of 50, 100, 250, 500, 750 and 1000 mA g^{-1}, respectively. Whereas for $Co(OH)_2$ NSs electrode, the achievable average specific reversible capacity values at these current densities are 862.9, 785.9, 553.8, 426.1, 303.7 and 246.2 mAh g^{-1}, respectively. Hence, at a current density of 1000 mA g^{-1}, $Co(OH)_2@MnO_2$ NSs electrode exhibit 1.43 times higher capacity value than $Co(OH)_2$ NSs electrode. As seen from the cyclic voltammograms, the $Co(OH)_2@MnO_2$ NS electrode has additional capacity from the MnO_2 phase, without compromising the capacity from the $Co(OH)_2$ NSs. The enhanced rate-capability of the $Co(OH)_2@MnO_2$ NSs electrode due to the synergistic effect between the active counterpart ($Co(OH)_2$ and MnO_2), which helps to improve electronic conductivity. To further prove the cycling stability of $Co(OH)_2@MnO_2$ NSs electrode at high current density, the electrode was cycled at a higher current density of 1000 mA g^{-1} up to 500 cycles as shown in Figure 8b. It shows the

stabilization of the reversible capacity to 420 mAh g^{-1} after 500 cycles and provides good cycling performance. Although there was an initial drop in specific capacity during cycling process, it still exhibits an excellent prolonged cycling stability. It is relevant to mention that the capacity fading is observed at all current densities, which might be due the high loading mass of our electrode. High capacities and stability has been reported for Mn_3O_4 and MoS_2, but the loading mass is lower than 0.5 mg cm^{-2} [21, 22].

Figure S3 shows the Nyquist plots of the $Co(OH)_2$ NSs (a) and $Co(OH)_2@MnO_2$ NSs anode. The lower values of R_s and R_{ct} for the $Co(OH)_2@MnO_2$ NSs anode in comparison to $Co(OH)_2$ NSs anode evident that the former has low internal resistance and fast charge transfer kinetics [35, 36]. Hence, it is important to mention that the deposition of MnO_2 NSs over $Co(OH)_2$ NSs could facilitate the charge transfer process at the electrode/electrolyte interface consequently decreasing the overall internal resistance of the cell. These result is in agreement with the improved lithium storage properties of $Co(OH)_2@MnO_2$ NSs over the $Co(OH)_2$ NSs.

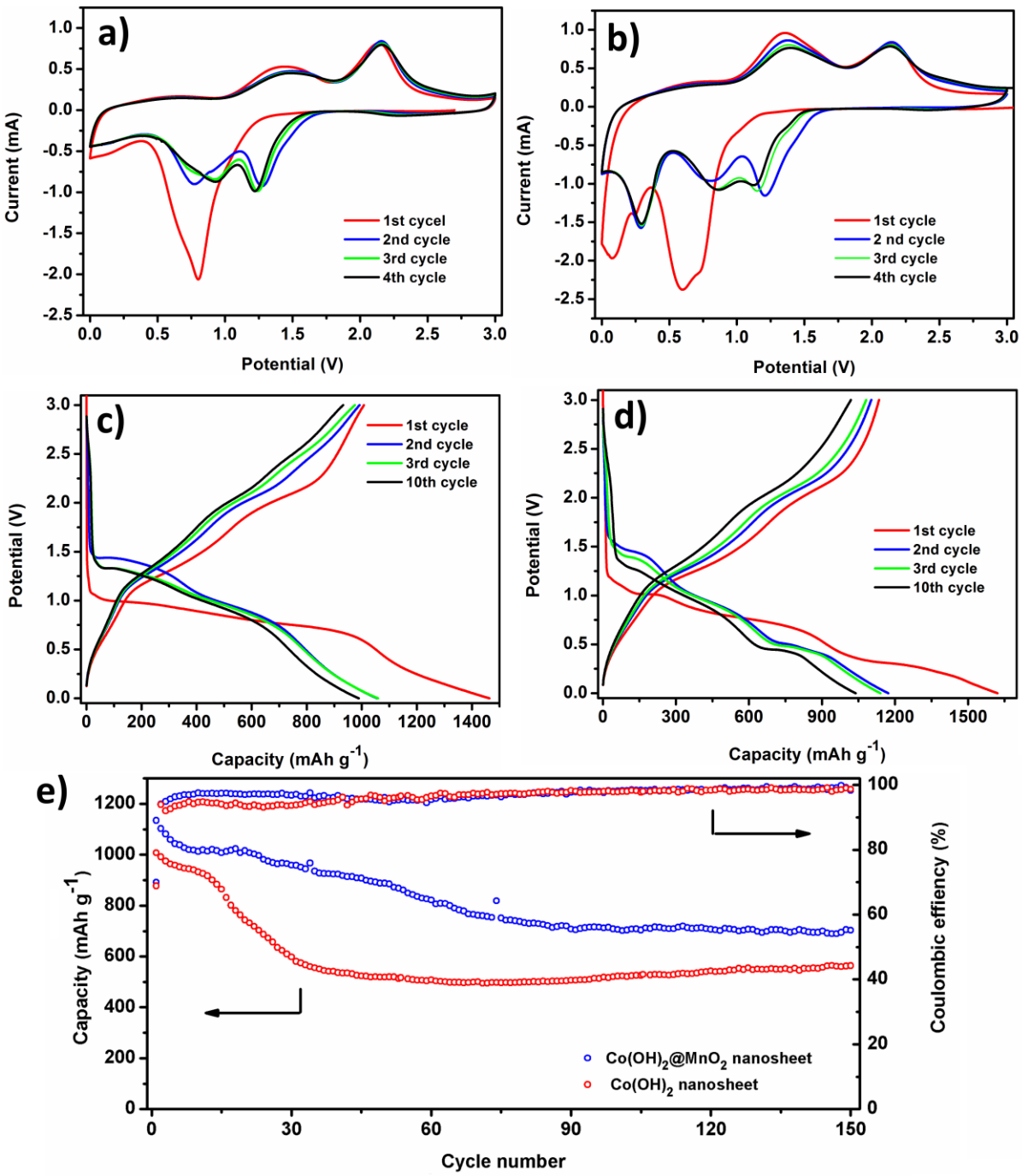

Figure 7. CV curves for the first four cycles at a scan rate of 0.1 mVs^{-1} between 0.0 V and 3.0 V of $Co(OH)_2$ NSs (a) and $Co(OH)_2@MnO_2$ NSs anode (b); Galvanostatic charge-discharge profiles for selective cycles at a current density of 250 mAg^{-1} of $Co(OH)_2$ NSs (c) and $Co(OH)_2@MnO_2$ NSs anode (d). (e) cycling performance at the current rate of 250 mA g^{-1}.

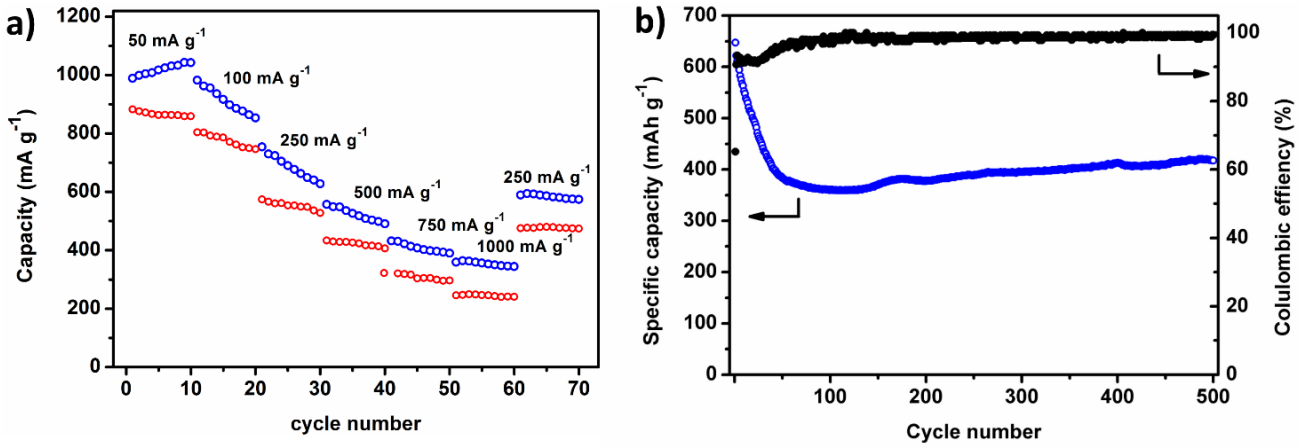

Figure 8. a) Discharge capacities of $Co(OH)_2$ NSs and $Co(OH)_2@MnO_2$ NSs anodes subjected to varying current densities between 0.0 and 3.0 V and (b) cycling performance of $Co(OH)_2@MnO_2$ NSs anodes at the current rate of 1000 mA g^{-1}.

Motivated by the superior performance of $Co(OH)_2@MnO_2$ NSs over $Co(OH)_2$ NSs, we further evaluate the supercapacitive performance of $Co(OH)_2@MnO_2$ NSs. The pseudocapacitive properties of $Co(OH)_2@MnO_2$ NSs electrodes are demonstrated by CV at different scan rate and galvanostatic charge-discharge measurements at different current densities in three electrode configurations.

Fig. 9a. presents the galvanostatic charge-discharge (GCD) curves of the $Co(OH)_2@MnO_2$ NSs arrays electrode in a potential window of 0–0.5 V at various current densities (20–50 A g^{-1}). Almost symmetrical nature of the GCD curves at all current densities indicating the outstanding electrochemical reversibility.

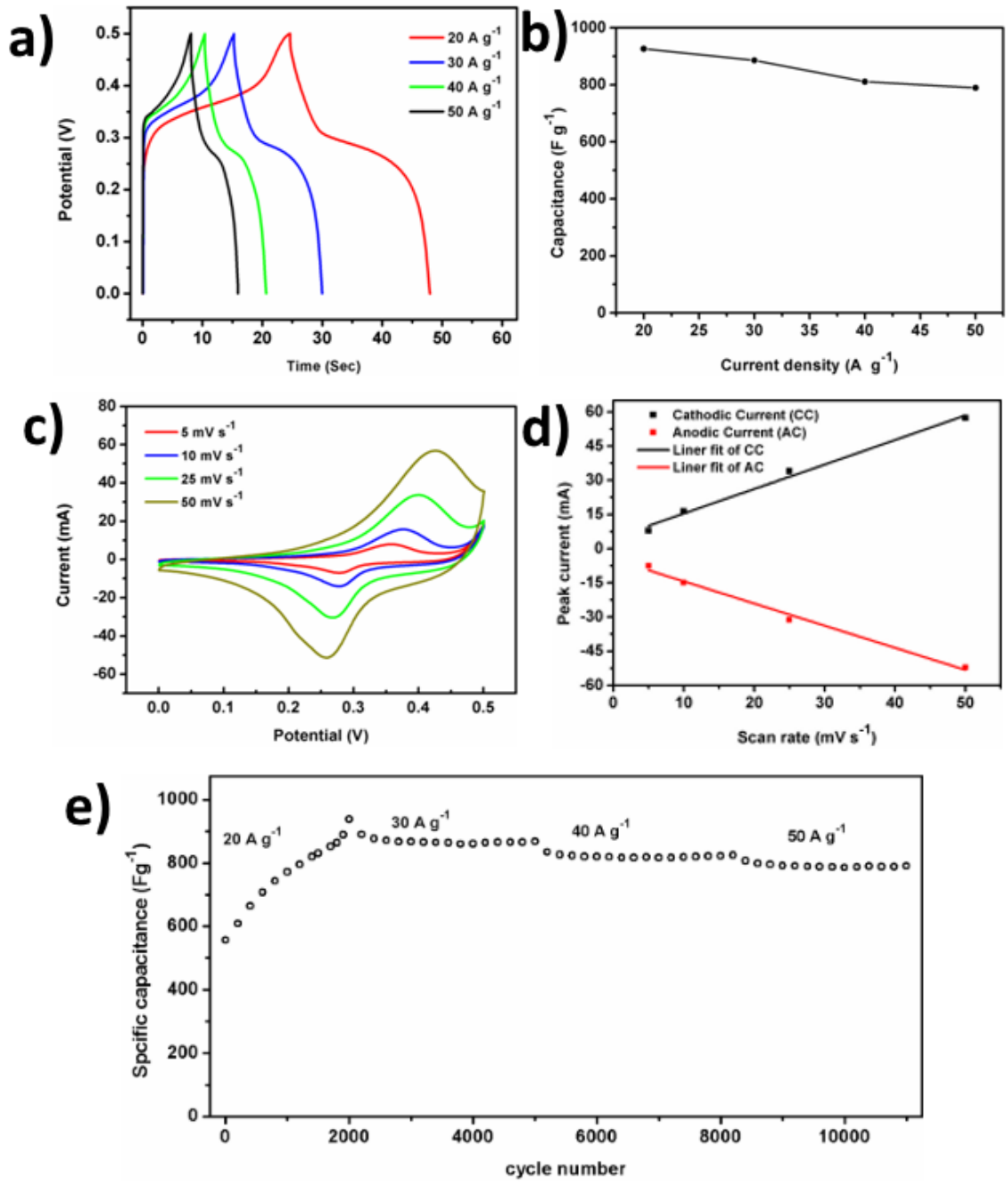

Fig. 9. (a) GCD curves of the $Co(OH)_2$@MnO_2 NSs arrays electrode at different current densities of 20–50 A g^{-1}. (b) Specific capacitances at different current densities of 120–50 A

g^{-1}. (c) CV curves of the $Co(OH)_2@MnO_2$ NSs arrays electrode at different scan rates of 5–50 mVs^{-1}. (d) Cycling performance at different densities 20–50 A g^{-1}.

To investigate the rate capability of the $Co(OH)_2@MnO_2$ NSs arrays electrode, the galvanostatic charge-discharge measurements performed at various current densities are shown in Fig. 9a. The corresponding calculated specific capacitances of the $Co(OH)_2@MnO_2$ NSs arrays electrode are 927 F g^{-1}, 886 F g^{-1}, 811 F g^{-1} and 791 F g^{-1} corresponding to the discharge current densities of 20 A g^{-1}, 30 A g^{-1}, 40 A g^{-1} and 50 A g^{-1}, respectively (Fig. 9b). With the increase applied current density, specific capacitance gradually decreased because of the incremental voltage fall and inadequate active material taking part in the redox reaction at a higher current density. Still, nearly 85.3% of the initial capacitance remained even after increasing the current density from 20 to 50 A g^{-1}. This excellent rate capability is ascribed to the thin structure of the interconnected NSs with the open space and the presence of surface pores which are serving as electrolyte reservoirs to shorten the ionic diffusion path and providing more active sites. The well-defined redox peaks in CV at all the current rates, suggesting the capacitive characteristics of Faradic redox reaction in the composite electrodes and the electrochemical reaction could be expressed as follows [35, 36]:

$Co(OH)_2 + OH^- \rightarrow CoOOH + H_2O + e^-$

$MnO_2 + K^+ + e^- \leftrightarrow MnOOK$

The increasing trend in peak current with an increase in the scan rate confirms that the kinetics of interfacial faradic redox reactions and the rates of electronic and ionic transport are rapid enough at the present scan rates [37]. Additionally, the clear redox peaks during charging and discharging, further suggesting the battery-type electrochemical behavior of $Co(OH)_2@MnO_2$ NSs arrays electrode [38-40]. Fig. 9d shows the variation of cathodic and

anodic peak currents as a function of the scan rate which indicates a diffusion-controlled process of OH^- with rapid redox reactions [41].

As the cycling stability of supercapacitor is one of the key parameter for commercial application, the cycling stability test of $Co(OH)_2$@MnO_2 NSs arrays electrode was carried out at different applied current densities continuously up to 10, 000 cycles and presented in Fig.9d. As shown in Fig. 9d. when cycling at 20 A g^{-1}, the capacitance value increases with cycle number which could be related to the improvement of improved surface wetting and gradual activation of the $Co(OH)_2$@MnO_2 NSs arrays electrode with time [41]. This type of increase in capacitance is also observed in other binder-free electrodes such as graphene, amorphous MoS_x, Co_3O_4 etc. This phenomenon can be explained based on the "electroactivation" of electrode materials via continuous ion interclation/deintercalation, which leads to partial re-exfoliation process [42-44]. The calculated capacitance values are 984 F g^{-1} (after 2000 cycles), 868 F g^{-1} (after 5000 cycles), 825 F g^{-1} (after 8200 cycles) and 790 F g^{-1} (after 10,000 cycles) corresponding to the discharge current densities of 20 A g^{-1}, 30 A g^{-1}, 40 A g^{-1} and 50 A g^{-1}, respectively.

Conclusions

In this work, we designed advanced hybrid electrode: $Co(OH)_2$@MnO_2 NSs arrays directly grown on nickel foam by two-step electro-deposition method. As an electrode for Li-ion batteries, the composite material exhibits a decent reversible capacity, excellent rate capability and appreciable cycling stability. The good lithium storage performance of this hybrid electrode results from the synergistic effect from two active materials ($Co(OH)_2$ and MnO_2), as the MnO_2 phase contributes to the capacity at lower voltages than the $Co(OH)_2$ phase, and without compromising the lithium storage of the latter.

When tested with respect to application as supercapacitor electrodes, the $Co(OH)_2$@MnO_2 NSs arrays delivers very high specific capacitance of 984 F g^{-1} (after 2000 cycles), 868 F g^{-1}

(after 5000 cycles), 825 F g^{-1} (after 8200 cycles) and 790 F g^{-1} (after 10,000 cycles) at discharge current densities of 20 A g^{-1}, 30 A g^{-1}, 40 A g^{-1} and 50 A g^{-1}, respectively. The excellent performance is attributed to the unique structural feature, presence of mesopores on the surface of nanosheets and the intimate contact between the nanosheets and the current collector. Therefore, the $Co(OH)_2$@MnO_2 NSs array electrode provides a promising option as super capacitors electrodes. The results also shows that the electrodeposition method is suitable for the fabrication of hybrid, binder free nano-arrays, and it is expected to be applicable for other bicomponent metal oxide-based nanostructures.

Acknowledgements

Authors greatly acknowledge the financial support by NTNU, Norway.

References

[1] P. Poizot, S. Laruelle, S. Grugeon, L. Dupont and J.M. Tarascon, *Nature*, 2000, 407, 496–499.

[2] G. Q. Zhang, H.B. Wu, H.E. Hoster, M.B. Chan-Park and X.W. Lou, *Energy Environ Sci* 2012, 5, 9453-9456.

[3] M. Kundu, G. Karunakaran, E. Kolesnikov, V. E. Sergeevna, S. Kumari, Mikhail V. Gorshenkov, D. Kuznetsov, *J.Ind. Eng. Chem.*, 2018, 59, 90-98.

[4] Y. Qin, Q. Li, J. Xu, X. Wang, G. Zhao, C. Liu, X. Yan, Y. Long, S. Yan and S. Li, *Electrochimica Acta*, 2017, 224, 90–95.

[5] D. Li, G. Li, H. Ge, J. Zhang and X. Meng, *New J. Chem.*, 2017, 41, 15501-15507.

[6] I. K. Durga, S S. Rao, J.-W. Ahn, T.-Y. Park, B. J.-Soo, C.-I. Ho, K. Prabakar and H.-J. Kim, Energies, 2018, 11, 1624

[7] X. Wang, H. Xia, J. Gao, B. Shi, Y. Fang and M. Shao, *J. Mater. Chem. A*, 2016, 4, 18181–18187.

[8] M. Kundu, G. Karunakaran, E. Kolesnikov, A. Dmitry, M. V. Gorshenkov and D. Kuznetsov, *Microporous Mesoporous Mater*. 2017, 247, 9-15.

[9] L. Lin, S. Tang, S. Zhao, X. Peng and N. Hu, *Electrochimica Acta*, 2017, 228, 175–182.

[10] X. Zheng, Y. Ye, Q. Yang and B. Geng, X. Zhang, *Dalton Trans.*, 2016, 45, 572–578.

[11] C. Kim, J. W. Jung, K. R. Yoon, D.-Y. Youn, S. Park and Il-Doo Kim, *ACS Nano*, 2016, 10, 11317−11326.

[12] J. Lin, H. Wang, Y. Yan, X. Zheng, H. Jia, J. Qi, J. Cao, J. Tu, W. Fei, J. Feng, *J. Mater. Chem. A*, 2018, 6, 19151-19158.

[13] J. Gou, S. Xie, Z. Yang, Y. Liu, Y. Chen, Y. Liu, C. Liu, *Electrochimica Acta*, 2017, 229, 299-305.

[14] J. Lin, X. Zheng, Y. Wang, H. Liang, H Jia, S. Chen, J. Qi, J. Cao, W. Fei, J. Feng, Inorg. Chem. Front., 2018,**5**, 1985-1991.

[15] Z. Q. Li, B. Li, L. W. Yin and Y. X. Qi, *ACS Appl. Mater. Interfaces*, 2014, 6, 8098–8107.

[16] A. A. AbdelHamid, Y. Yu, J. Yang and J. Y. Ying, *Adv. Mater.* 2017, 29, 1701427

[17] X. Wang, Y. Chen, O. G. Schmidt and C. Yan, *Chem. Soc. Rev.* 2016, 45, 1308-1330.

[18] J. Deng, X. Lu, L. Liu, L. Zhang and O. G. Schmidt, *Adv. Energy Mater.* 2016, 6, 1600797.

[19] M. Kundu, C. C. Albert Ng, D. Y. Petrovykh and L.F Liu, *Chem. Commun.*, 2013, **49**, 8459-8461.

[20] X. Liu, W. Si, J. Zhang, X. Sun, J. Deng, S. Baunack, S. Oswald, L. Liu, C. Yan and O. G. Schmidt, *Sci. Rep.* 2014, 4, 7452.

[21] X. Y. Fan, Y. Cui, P. Liu, L. Gou, L. Xu and D. L. Li, *Phys. Chem. Chem. Phys.*, 2016, 18, 22224-22234.

[22] Y. Zhou, Y. Liu, W. Zhao, F. Xie, R. Xu, B. Li, X. Zhou and H. Shen, *J. Mater. Chem. A*, 2016, 4, 5932-5941.

[23] Q. Chen, F. Lu, Y. Xia, H. Wang and X. Kuang, *J. Mater. Chem. A*, 2017, 5, 4075–4083.

[24] C. Zhu, G. Fang, Jiang Zhou, J. Guo, Z. Wang, C. Wang, J. Li, Y. Tang and S. Liang, *J. Mater. Chem. A*, 2018, 6, 9677-9683.

[25] S. Yu, Y. Zhang, G. Lou, Y. Wu, X. Zhu, H. Chen, Z. Shen, S. Fu, B. Bao and L. Wu, *Sci. Rep.*, 2018, 5246.

[26] M. Zhen, L. Liu and C. Wang, *Microporous Mesoporous Mater.* 2017, 246, 130-136.

[27] Y. Xiao, J. Huang, Y. Xu, H. Zhu, K. Yuan and Y. Chen, *J. Mater. Chem. A*, 2018, 6, 9161-9171.

[28] J. Yang, H. Liu, W.N. Martens and R. L. Frost, *J. Phys. Chem. C*, 2010, 114 (1), 111–119.

[29] M. C. Biesinger, B. P.Payne, A. P.Grosvenor, L. W.M.Lau, A. R.Gerson and R. St.C.Smart, Applied surface science, 2011, 257, 2717-2730.

[30] Y. Zhao and P. Jiang, *Colloids and Surfaces A: Physicochem. Eng. Aspects*, 2014, 444, 232–239.

[31] W. Cao and W. Wang, *Mater. Lett.*, 2016, 185, 495–498.

[32] D. Larcher, C. Masquelier, D. Bonnin, Y. Chabre, C. Masson, J.-B. Leriche and J.-M. Tarascon, *J. Electrochem. Soc., 2003*, 150, A133-A139.

[33] J. Zhou, J. Li, K. Liu, L. Lan, H. Song and X. Chena, *J. Mater. Chem. A*, 2014, 2, 20706-20713.

[34] T. Wu and K. Liang, *RSC Adv.*, 2016, 6, 15541-15548.

[35] Z. Yu, Z. Cheng, Z. Tai, X. Wang, C. M. Subramaniyam, C. Fang, S. Al-Rubaye, X. Wang and S. Dou, *RSC Adv.*, 2016, 6, 45783–45790.

[36] X. Liu, G. Sheng, M. Zhong and X. Zhou, *Nanoscale*, 2018,10, 4209-4217

[37] J. Lin, H. Wang, X. Zheng, Y. Du, C. Zhao, J. Qi, J. Cao, W. Fei, J. Feng, *J. Power Sources*, 2018, 401, 329-335.

[38] V. Augustyn, P. Simon and B. Dunn, *Energy Environ. Sci.* 2014, 7, 1597–1614.

[39] M. Ulaganathan, M. Maharjan, Q. Yan, V. Aravindan and S. Madhavi, *Chem. Asian* J.10.1002/asia.201700707.

[40] X.-J. Ma, W.-B. Zhang, L.-B. Kong, Y.-C. Luo and L. Kang, *New J. Chem.*, 2015, 39, 6207-6215.

[41] M. Kundu and L. Liu, *Mater. Lett.* 2015, 144, 114–118.

[42] J. Lin, H. Jia, H. Liang, S. Chen, Y. Cai, J. Qi, C. Qu, J. Cao, W. Fei, J. Feng, *Adv. Sci.* 2018, 5, 1700687.

[43] J. Lin, H. Jia, H. Liang, S. Chen, Y. Cai, J. Qi, C. Qu, J. Cao, W. Fei, J. Feng, *Chemical Engineering Journal*, 2018, 5, 562-569.

[44] M. Li, W. Yang, Y. Huang and Y. Yu, *Sci China Mater* 2018, 61(9), 1167–1176

[45] M. Beidaghi and C. Wang, *Adv. Funct. Mater.*, 2012, 22, 4501–4510.

[46] S. K. Balasingam, A. Thirumurugan, J. Sung Lee and Y. Jun, ***Nanoscale***, 2016,**8**, 11787-11791.

[47] Z. Yu, Z. Cheng, Z. Tai, X. Wang, C. M. Subramaniyam, C. Fang, S. Al-Rubaye, X. Wang and S. Dou, RSC Adv., 2016, 6, 45783–45790.